Plasticity-induced repression of Irf6 underlies acquired resistance to cancer immunotherapy

Il-Kyu Kim
University of Pennsylvania
Mark Diamond
University of Pennsylvania
Salina Yuan
University of Pennsylvania
Samantha Kemp
University of Pennsylvania
Qinglan Li
University of Pennsylvania
Jeffrey Lin
University of Pennsylvania https://orcid.org/0000-0002-2518-6863
Jinyang Li
University of Pennsylvania
Robert Norgard
University of Pennsylvania
Stacy Thomas
University of Pennsylvania https://orcid.org/0000-0002-6703-5246
Maria Merolle
University of Pennsylvania
Takeshi Katsuda
University of Pennsylvania
John Tobias
University of Pennsylvania https://orcid.org/0000-0002-5362-7013
Katerina Politi
Yale University
Robert Vonderheide
University of Pennsylvania https://orcid.org/0000-0002-7252-954X
Ben Stanger (bstanger@upenn.edu)
University of Pennsylvania https://orcid.org/0000-0003-0410-4037

Article

Keywords:

Posted Date: June 1st, 2023

DOI: https://doi.org/10.21203/rs.3.rs-2960521/v1

Abstract

Acquired resistance to immune checkpoint immunotherapy remains a critical yet incompletely understood biological mechanism. Here, using a mouse model of pancreatic ductal adenocarcinoma (PDAC) to study tumor relapse following immunotherapy-induced responses, we found that tumors underwent an epithelial-to-mesenchymal transition (EMT) that resulted in reduced sensitivity to T cell-mediated killing. EMT-transcription factors (EMT-TFs) ZEB1 and SNAIL function as master genetic and epigenetic regulators of this tumor-intrinsic effect. Acquired resistance was not due to immunosuppression in the tumor immune microenvironment, disruptions in the antigen presentation machinery, or altered expression of immune checkpoints. Rather, EMT was associated with epigenetic and transcriptional silencing of interferon regulatory factor 6 (*Irf6*), which renders tumor cells less sensitive to the pro-apoptotic effects of TNF-α. These findings show how resistance to immunotherapy in PDAC can be acquired through plasticity programs that render tumor cells impervious to T cell killing.

Introduction

Immune checkpoint blockade (ICB) has transformed cancer treatment for multiple malignancies[1, 2], but durable clinical responses remain elusive in many patients. Acquired resistance to immunotherapy represents an important clinical challenge. For example, approximately one third of patients with metastatic melanoma who had objective responses to ICB in a recent clinical trial subsequently relapsed over ~2 years of continuous therapy[3]. Similarly, although PD-1 and PD-L1 therapeutic blockade has revolutionized treatment of patients with non-small cell lung cancer (NSCLC), relapse after initial response is a major challenge[4].

Unlike primary resistance, which is attributable to factors present when therapy is initiated, acquired resistance emerges over time. In patients treated with targeted therapies (e.g. EGFR inhibition), acquired resistance is often associated with cellular plasticity, a phenomenon that broadly describes changes in cell identity along a phenotypic spectrum[5]. One of the most well studied examples of cellular plasticity is epithelial-to-mesenchymal transition (EMT), during which carcinoma cells lose their epithelial features and acquire the more motile characteristics of fibroblasts and leukocytes[6, 7]. In addition to its phenotypic effects on tumor cells, EMT has also been associated with the development of an immunosuppressive TME in NSCLC, breast cancer, and melanoma[8-11]. These findings have implications for immunotherapy, as exemplified by a recent report that the EMT transcription factor SNAIL promotes primary resistance to ICB in breast carcinomas, most notably through the CD73 pathway[12].

Studies of acquired resistance to immunotherapy have been difficult due to a lack of tractable biological systems with which to model tumor relapses over prolonged periods of time. Here, we present an immunotherapy-sensitive model of pancreatic ductal adenocarcinoma (PDAC) in which recurrent (and therapy-resistant) disease appears weeks-to-months after a complete response to treatment, and delineate underlying cellular and molecular mechanisms.

RESULTS

A model for acquired immunotherapy resistance

Pancreatic cancer is known to respond poorly to ICB. However, a fraction of patients with PDAC clinically respond to combinations including chemotherapy, ICB, and CD40 agonist[13,14], similar to observations in the KPC model system[15–17]. To establish a model of acquired resistance in this setting, we evaluated the efficacy of various chemo- and immuno-therapy drug regimens in subcutaneously implanted 4662 cells[17] derived from the KPC mouse model of PDAC (*Kras*$^{LSL-G12D/+}$; *Trp53*$^{LSL-R172H/+}$; *Pdx1*-Cre). Indeed, neither chemotherapy with gemcitabine (G) and nab-paclitaxel (A), nor ICB with anti-CTLA-4 Ab (C) and anti-PD-1 Ab (P) had significant antitumor effects (**Extended Data** Fig. 1a), as we previously reported[17,18]. However, combination regimens that included agonistic anti-CD40 Ab (F) resulted in tumor regressions and prolonged survival, including complete responses (CRs) (Fig. 1a, b and **Extended Data** Fig. 1a). Antitumor responses were associated with immunological memory that was dependent upon T cells but not NK cells (**Extended Data** Fig. 1b–d). Thus, the combination of CD40 agonist and ICB leads to durable CRs and T cell memory in PDAC.

Despite the potent antitumor activity elicited with combination therapy, responses were heterogenous among treated mice and could be categorized as follows: (i) mice that did not respond initially, reflecting primary resistance; (ii) mice in which therapy delayed tumor growth but did not induce full regression; (iii) mice that fully regressed and then spontaneously relapsed afterwards, reflecting acquired resistance; and (iv) mice exhibiting a durable CR (Fig. 1a–c). Importantly, tumors that recurred after an initial CR or near CR displayed acquired resistance to therapy, since retreatment with combination therapy yielded no responses (Fig. 1d). We therefore hypothesized that recurrent tumors, particularly those with a late escape phenotype, represented tumors that have evaded therapy-induced T cell surveillance and maintain a stable resistant state.

To test this hypothesis, we established tumor cell lines from cohorts of mice that had different therapeutic outcomes following combination therapy. We first compared therapy responses by re-inoculating each tumor cell line into naïve mice and administering combination therapy. Cell lines derived from non-responsive tumors (termed “Early Progressor (EP) lines”, $n = 2$) gave rise to tumors exhibiting variable responses to combination therapy, with rates of regression and CR that were comparable to mice bearing control cell lines that were never exposed to therapy (termed “Ctrl lines”, $n = 4$) (Fig. 1e–g). By contrast, cell lines derived from tumors that underwent CR followed by relapse (termed “Escape (Esc) lines”, $n = 8$) gave rise to resistant tumors exhibiting poor survival (Fig. 1e–g). These results suggest that the mechanisms allowing tumors to grow after therapy-induced CR (i.e. acquired resistance) persist in the Esc lines, whereas the mechanisms that render tumors non-responsive upon first exposure to immunotherapy (i.e. primary resistance) are not stably preserved in the EP lines.

EMT confers immunotherapy resistance in PDAC

We considered two models that could explain the emergence of resistant tumors. First, tumor escape might have resulted from the selective expansion of pre-existing resistant clones. Alternatively, cell plasticity, in the setting of immunotherapy, might have fostered the emergence of newly resistant clones. To distinguish between these models, we generated clonal PDAC lines from the 4662 parental line and examined therapy responses. Consistent with our earlier findings with the 4662 parental line, individual clones exhibited heterogeneous therapeutic outcomes including escape tumors following CRs (**Extended Data** Fig. 1e), suggesting that tumor cell plasticity, rather than presence of pre-existing clones, accounts for the resistant phenotype. As expected, clonal tumors that escaped following an immunotherapy-induced CR (C10.e1 and C7.e1) were highly resistant to combination therapy compared to control tumors (**Extended Data** Fig. 1f).

Next, we set out to understand the mechanisms underlying acquired resistance. We began by performing bulk RNA sequencing on parental 4662 cells, EP cells, and Esc cells. Principle component analysis (PCA) revealed a strong similarity between parental cells and EP cells, while Esc cells diverged from both, suggesting that Esc cells had acquired a unique transcriptional profile (Fig. 2a). We also observed striking morphological differences; namely, parental cells exhibited epithelial features and gave rise to well-differentiated tumors, while Esc cells exhibited spindle-like features and gave rise to poorly differentiated tumors (Fig. 2b and **Extended Data** Fig. 1g). In accordance with these observations, gene set enrichment analysis (GSEA) showed that Esc cells were highly enriched for the Hallmark EMT gene signature compared to parental tumors (Fig. 2c) and exhibited a decrease in mRNAs associated with the epithelial phenotype and an increase in mRNAs associated with the mesenchymal phenotype (**Extended Data** Fig. 1h, 2a). In addition to EMT, which was the most significantly enriched gene set in Esc tumors, other gene sets enriched in Esc tumors included interferon response, angiogenesis, hypoxia, and inflammation response, while gene sets that were reduced in Esc tumors included androgen/estrogen response and cholesterol homeostasis (**Extended Data** Fig. 2b). These findings suggest that Esc tumors exhibit transcriptional hallmarks of EMT.

Given the well-documented role of EMT in various forms of therapy resistance[19], we hypothesized that EMT was not merely correlated with acquired resistance to immunotherapy but was itself acting as a driver of resistance. To test this, we assessed whether gain- or loss-of-function of the *Zeb1* and *Snail* EMT-TFs alters the response to immunotherapy (CD40 agonist plus ICB). First, we confirmed that overexpression of *Zeb1* and *Snail* in parental tumors, or ablation of both genes in Esc tumors, prompted the expected changes in epithelial-mesenchymal phenotype and morphology (**Extended Data** Fig. 2c–f). Next, we performed RNA sequencing of the engineered lines. GSEA revealed that *Zeb1* and *Snail* overexpression in parental tumors (*Zeb1/Snail* OE) resulted in the enrichment of gene signatures associated with Esc tumors *in vitro* and *in vivo* (Fig. 2d, e), indicating that the transcriptional changes induced by these EMT-TFs resemble those associated with acquired resistance to immunotherapy. Consistent with these findings, *Zeb1/Snail* OE tumors exhibited reduced responses to immunotherapy compared to EV-transduced controls, resulting in poorer survival (Fig. 2f, g). By contrast, ablation of *Zeb1* and *Snail* (*Zeb1*$^{-/-}$*Snail*$^{-/-}$) in Esc tumors rescued the response to immunotherapy, leading to greater

survival in treated mice (Fig. 2h, i). Importantly, none of the tumor cell lines tested above had a defect in cell growth *in vitro* (**Extended Data** Fig. 2g–i). Taken together, these data support the hypothesis that EMT promotes acquired resistance to immunotherapy.

EMT drives tumor cell-intrinsic resistance to cytotoxic T cell activity

Resistance to immunotherapy in various PDAC models has been associated with an immunosuppressive TME characterized by abundant granulocytic myeloid-derived suppressor cells (gMDSCs) and a paucity of dendritic cells (DCs) and CD8 T cells[16, 20, 21]. To determine whether EMT fostered the creation of an immunosuppressive TME, we compared the immune profiles associated with parental, Esc, and *Zeb1/Snail* OE tumors. Contrary to expectations, both Esc and *Zeb1/Snail* OE tumors exhibited decreased infiltration of gMDSCs and increased infiltration of $CD103^+$ DCs (cDC1) and $CD8^+$ T cells compared to parental tumors (Fig. 3a–c). Similar results were observed in the orthotopic setting (**Extended Data** Fig. 3a, b), suggesting that EMT has similar effects on the TME regardless of the site of injection. Likewise, the expression of co-inhibitory molecules such as PD-L1 and CD73 was reduced in both Esc and *Zeb1/Snail* OE tumors, although the expression of the TIGIT ligand CD155 was slightly increased compared to parental controls (**Extended Data** Fig. 3c, d). Conversely, ablation of *Zeb1* and *Snail* in Esc tumors resulted in a paradoxical increase in immunosuppressive gMDSCs and a decrease in total T cells (**Extended Data** Fig. 3e). These results suggest that EMT promotes resistance to immunotherapy by mechanisms other than the creation of an immunosuppressive TME.

To determine whether loss of MHC I and/or Ag presentation accounted for acquired resistance in our model, we transduced parental and Esc tumor cells with chicken *ovalbumin* (OVA) and assessed the relative intensity of antigen presentation using an antibody (Anti-H-$2K^b$ bound to SIINFEKL) that detects OVA peptide in the context of MHC class I. Although Esc lines exhibited mild heterogeneity in antigen presentation (some slightly increased and some slightly decreased compared to parental; **Extended Data** Fig. 4a), all OVA-expressing Esc lines exhibited marked resistance to killing when co-cultured with OVA-specific $CD8^+$ T cells (OT-I) (**Extended Data** Fig. 4b). Importantly, Esc and *Zeb1/Snail* OE tumors *in vivo* had comparable MHC I expression compared to parental control tumors (**Extended Data** Fig. 4c, d). These results suggest that mechanisms other than MHC I downregulation account for EMT-associated acquired resistance in PDAC.

T cells play a crucial role in limiting tumor relapse following tumor clearance[22–24]. We confirmed in our model that animals achieving immunotherapy-induced CRs required T cells, but not NK cells, to maintain tumor control (Fig. 3d, e). This suggested two possibilities: (i) EMT induces a tumor cell intrinsic resistance to T cell killing, and/or (ii) EMT in tumor cells induces a defect in T cell function. To explore these possibilities, we transplanted OVA-expressing parental and Esc tumor cells into NOD/SCID mice and measured tumor growth before and after infusion with activated OT-I cells. OVA-expressing parental tumors responded to the OT-I infusion with a slowing of tumor growth (Fig. 3f). However, OVA-expressing

Esc tumors grew at a similar rate despite the presence of OT-I (Fig. 3f). These results suggest that tumors escape immune surveillance by evading antigen-specific T cell immunity.

Next, we established an *in vitro* co-culture system to determine whether the mechanism of resistance involves a direct interaction between tumor cells and CD8 T cells. Whereas parental cells were killed in the presence of either activated or non-activated OT-I cells (measured as positivity for AnnexinV and 7-AAD), Esc cells were highly resistant to OT-I killing (Fig. 3g). Next, to determine whether resistance to killing was cell-autonomous, we labelled parental and Esc tumors with different fluorescent markers and co-cultured them individually or together with OT-I cells. In this mixed co-culture, Esc cells were far more resistant to killing than parental cells (Fig. 3h), suggesting that a tumor cell-intrinsic block to T cell killing drives the resistance phenotype. In addition, we found that naïve OT-I cells were poorly primed when co-cultured with Esc cells compared to parental cells (**Extended Data** Fig. 4e, f). Consistent with this finding, we noted that parental cells mixed with Esc cells had reduced cell death in OT-I co-culture compared to parental cells co-cultured alone (Fig. 3h, compare “Parental” to “Parental + Esc”). Taken together, these results indicate that Esc cells are intrinsically resistant to T cell killing and have a mild defect in T cell priming ability.

Because resistance arose in the setting of plasticity rather than outgrowth of a pre-existing resistant subclone (**Extended Data** Fig. 1e), we next studied whether the immune pressure present in the *in vitro* OT-I co-culture system might induce a similar change. Remarkably, parental cells that survived 2 days of co-culture exhibited reduced expression of the epithelial marker E-cadherin, suggestive of an EMT-like process (**Extended Data** Fig. 5a). To determine whether immunotherapy prompts a similar shift in epithelial-mesenchymal phenotypes *in vivo*, we implanted parental tumor cells and compared the transcriptional profiles of tumors treated for 2d to those of control (untreated) tumors. GSEA revealed that even this short-term immunotherapy caused tumor cells *in vivo* to become enriched for signatures associated with the Esc tumors and the Hallmark EMT signature (**Extended Data** Fig. 5b, c). Together, these findings strongly suggest that immune pressure selects for PDAC cells with a more mesenchymal phenotype that confers resistance to T cell killing. In line with this idea, we found that *Zeb1/Snail* OE rendered parental tumor cells resistant to killing by OT-I cells (Fig. 3i), whereas depletion of *Zeb1* and *Snail* made Esc tumor cells more sensitive to T-cell killing (Fig. 3j).

Transcriptional and epigenetic regulation of Irf6 contributes to acquired immunotherapy resistance

Given the stability of the EMT-associated resistance phenotype, we reasoned that the underlying mechanism was likely to involve epigenetic remodeling. Consequently, we performed ATAC-seq on parental and *Zeb1*/*Snail* OE tumors to identify genes whose chromatin accessibility changed upon EMT induction (in both steady state and in co-culture with OT-I cells) (Fig. 4a). In parallel, we examined the overlap of EMT-associated transcriptional differences across two experimental comparisons – (i) parental cells vs. Esc cells and (ii) EV- vs. *Zeb1*/*Snail*-transduced parental cells – and then used GSEA to

compile a list of candidate genes whose transcriptional regulation correlated with immune sensitivity across both datasets (**Supplementary Table 1**). An examination of these epigenetically and transcriptionally regulated gene lists yielded a single gene candidate common to both: interferon regulatory factor 6 (*Irf6*).

Based on these findings, we hypothesized that Irf6 plays a role in EMT-associated resistance to T cell killing. As predicted bioinformatically, *Zeb1*/*Snail* OE resulted in a loss of chromatin accessibility of the *Irf6* locus (Fig. 4b), particularly at the promoter region (Fig. 4c and **Extended Data** Fig. 6a, b), leading to a corresponding decrease in *Irf6* mRNA (Fig. 4d). In agreement with this finding, *Zeb1*/*Snail* OE also resulted in the downregulation of putative Irf6 target genes but not those of unrelated transcription factors such as *Six2* (Fig. 4e and **Extended Data** Fig. 6c–e). Next, using gene sets generated via ectopic expression of *Irf6* in PDAC cells, we found that Irf6 signatures were strongly enriched in therapy-sensitive parental and EV tumors compared to Esc and *Zeb1*/*Snail* OE tumors, respectively (Fig. 4f). Interestingly, an analysis of published human scRNA-Seq PDAC datasets revealed that *IRF6* expression is largely restricted to epithelial cells, in contrast to other *IRF* genes[25–27] (**Extended Data** Fig. 6f–h). Furthermore, IRF6 signatures from human PDAC were consistently enriched in therapy-sensitive parental and EV tumors (Fig. 4g). Taken together, these results nominate Irf6 as a candidate EMT-related driver of immune sensitivity whose loss is associated with acquired resistance to immunotherapy.

Irf6 restoration promotes cytotoxic T cell killing and response to immunotherapy in resistant PDAC

To functionally assess the role of Irf6 in acquired immunotherapy resistance, we restored *Irf6* expression to Esc tumors and assessed vulnerability to T cell killing *in vitro*. Esc tumor cells engineered to re-express *Irf6* regained sensitivity to T cell killing upon OT-I co-culture (Fig. 5a), whereas parental cells lacking *Irf6* (*Irf6*$^{-/-}$) became resistant to OT-I cell killing (Fig. 5b). Of note, although *Irf6*-expressing Esc cells maintained their mesenchymal morphology and had similar growth kinetics in culture (**Extended Data Fig. 7a, b**), epithelial genes such as Ecad, Ocln, and Cldn7 were upregulated compared to control (EV) cells (**Extended Data Fig. 7c**). Next, we tested the ability of *Irf6* expression to restore immunotherapy responsiveness *in vivo*. Esc tumors expressing *Irf6* partially recovered their response to immunotherapy compared to control (EV) tumors, with some mice exhibiting durable CRs and prolonged survival (Fig. 5c, d). These results suggest that loss of *Irf6* in association with EMT promotes resistance to T cell killing *in vitro* and responses to immunotherapy *in vivo*, phenotypes that can be rescued by restoration of *Irf6* expression.

To determine whether *IRF6* might be associated with acquired resistance to immunotherapy in patients, we identified a dataset in which pre- and post-treatment transcriptome data were available from lung cancer patients who had initially responded to ICB but later developed resistance[28]. Roughly half of the patients with acquired resistance exhibited decreased expression of *IRF6* compared to pre-treatment levels; in those patients, *Irf6* signatures were enriched in pre-treatment samples (pre-ICB) compared to

those with acquired immunotherapy resistance (IR) (Fig. 5e, f). Importantly, EMT signatures were inversely correlated with *IRF6* expression, such that therapy-resistant patients with decreased *IRF6* expression were enriched for EMT signatures compared to pre-treatment (Fig. 5g). By contrast, therapy-resistant patients with no change or an increase in *IRF6* expression showed the opposite result (Fig. 5g). Thus, immunotherapy resistance in a subset of lung cancer patients is associated with loss of *IRF6* expression and concomitant acquisition of an EMT signature.

Irf6 facilitates T cell-mediated tumor control via TNF-induced apoptosis

To understand how *Irf6* regulates tumor cell-intrinsic resistance to T cell killing, we compared the transcriptomes of control (EV) and *Irf6*-expressing tumor cells after OT-I co-culture. GSEA identified various hallmark gene sets as enriched (cholesterol homeostasis, MYC targets, estrogen response, TNF-α signaling via NFκB, etc.) or depleted (IFN response and EMT) following ectopic expression of *Irf6* (**Extended Data Fig. 7d**). Given the known role of TNF and NF-κB in T cell-mediated killing of target cells[29–31], we hypothesized that *Irf6* loss confers resistance to T cell killing by blocking the pro-apoptotic effects of TNF-α. Consistent with this hypothesis, we found that Esc cells were markedly resistant to TNF-α-induced cell death compared to parental cells and *Irf6* re-expression restored sensitivity to TNFα-induced killing (Fig. 6a). Re-expression of *Irf6* in Esc cells had no detectable effect on NF-κB pathway components (**Extended Data Fig. 7e**). TNF-α-induced killing was due to apoptosis, as *Irf6*-expressing cells exhibited greater staining for cleaved caspase-3 compared to control (EV) Esc cells, both *in vitro* following TNF-α treatment (Fig. 6b) and *in vivo* following immunotherapy (Fig. 6c). Treatment with the pan-caspase inhibitor z-VAD reversed the enhanced sensitivity to TNF-α of *Irf6*-expressing cells (Fig. 6d), and deletion of *Tradd*, *Fadd*, or *Casp8* – genes encoding intracellular mediators of TNF-induced cell death – had similar effects (Fig. 6e).

T cells employ multiple redundant mechanisms to kill their targets. To confirm that death receptor signaling is critical for T cell cytotoxicity of PDAC cells, we assessed the consequences of *Tradd*, *Fadd*, or *Casp8* deletion on T cell-mediated cytotoxicity. Whereas *Irf6* expression restored the ability of OT-I cells to kill OVA-expressing Esc cells, loss of any of these apoptosis mediators significantly blunted the effect (Fig. 6f), suggesting that this pathway plays an important role in T cell killing of these PDAC cells. Finally, we used TNF-α neutralizing Ab to determine whether the dependency on Irf6 for efficient T cell killing was specific for TNF-α. Whereas anti-TNF-α antibodies had no effect on T cell-mediated killing of control Esc cells in OT-I co-culture, antibody treatment reduced the killing of *Irf6*-expressing cells to the level of control Esc cells (Fig. 6g). Thus, Irf6 sensitizes PDAC cells to T cell-mediated apoptosis by altering the cellular response to TNF.

IRF6-related disorders in humans, including Van Der Woude syndrome, have been linked to point mutations in the *IRF6* DNA binding domain[32]. These mutations introduced into the mouse *Irf6* gene either partially or completely abrogated Irf6's ability to sensitize cells to TNF-α-induced killing (**Extended Data**

Fig. 7f), indicating a role for DNA binding in Irf6's effects. Together, these results suggest that Irf6 confers sensitivity to TNF-induced cytotoxicity through a classical TRADD-FADD-CASP8 death receptor signaling pathway.

Discussion

While predictors of primary resistance to immunotherapy in patients have been studied in detail[33–35], there has been far less investigation of acquired resistance[36]. Our results suggest that distinct mechanisms operate in the two settings: whereas primary resistance is typically associated with a paucity of T cells and an immunosuppressive TME[16], acquired resistance is paradoxically associated with a hyperimmune TME, where resistance to T cell-mediated cytotoxicity occurs through a change in cell state. Our data suggest that epithelial plasticity (EMT) confers resistance by providing PDAC cells with an intrinsic resistance to T cell killing rather than by assembling an immunosuppressive tumor microenvironment. Mechanistically, EMT drives repression of *Irf6*, making the tumor cells less susceptible to the pro-apoptotic effects of T cell-derived TNF-α.

Preclinical and clinical studies by us and others have provided encouraging results from combination therapies that include CD40 agonists[13–15, 17, 18, 37]. These studies, and our results here, indicate that therapy responses are heterogenous, reflecting various resistance programs. Oncogenic signaling, defects in Ag presentation, and immune-suppressive elements of the TME are known to induce primary resistance, whereas the mechanisms of acquired resistance are poorly understood and likely involve strategies distinct from those used by primary tumors[38]. This concept is reinforced by our finding that Esc tumors with acquired resistance exhibited a paradoxical increase in $CD8^+$ T cell infiltration, a reduction in gMDSC infiltration, and a decrease in the expression of the co-inhibitory molecules PD-L1 and CD73 – effects that would all be predicted to enhance rather than diminish antitumor immunity. These findings suggest that once a tumor has responded to immunotherapy, it activates mechanisms other than a reconfiguration of the TME to evade further immune attack.

An inverse relationship between EMT and immunotherapy response has been well-documented in mice and humans[8, 10–12, 39–41]. Our finding that EMT blunts the tumor cell's response to T cell-derived TNF-α is in line with previous reports implicating TNF-mediated killing as a crucial mechanism of tumor elimination, especially in poor neoantigen-expressing tumors[30, 42]. Accordingly, genetic ablation or pharmacological inhibition of the TRAF2/cIAP complex, which facilitates TNF-induced cell death, resulted in improved antitumor responses when combined with ICB in preclinical studies[31, 43, 44]. In the context of these studies, our work suggests that strategies that re-establish sensitivity to death receptor-mediated killing, as reported recently in the setting of tumor cell intrinsic resistance to CAR T cell killing[45], may reverse or prevent the emergence of resistance after an initial response to immunotherapy.

Our study revealed acquired resistance to be the product of plasticity rather than the outgrowth of pre-existing mutant subclones. This finding is consistent with studies of targeted therapies such as BRAF

inhibition, where acquired resistance can result from the outgrowth of rare subclones (i.e. cells carrying with mutations in the drug target) and/or non-genetic cell state transitions that enable the outgrowth of cells that are resistant on the basis of an altered phenotype[46]. Indeed, we found that co-culturing OVA-expressing tumor cells with antigen-specific T cells for just 2 days resulted in a profound activation of EMT programs in the surviving cells (**Extended Data** Fig. 5). While we believe this is likely due to the selective outgrowth of cells with a more mesenchymal phenotype (i.e. preferential killing of cells with a more epithelial phenotype), we cannot rule out the possibility that T cells may also possess EMT-inducing properties.

The Irf family of transcription factors have broad activities in immune function that extend beyond their originally described role in type 1 interferon responses[47]. Unlike other Irf family members, Irf6's known roles are limited to the proliferation and function of epithelial (epidermal) cells[32, 48]. In humans, heterozygous mutations in *IRF6* are associated with van der Woude syndrome, a condition associated with facial malformations due to developmental dysmorphogenesis[49]. Our data show that EMT leads to the repression of *Irf6* – either during spontaneous EMT in Esc cells or EMT induced by the expression of *Zeb1* and *Snail*. *Irf6* ablation in parental cells protects them from T cell killing, while *Irf6* restoration leads to greater T cell killing and immunotherapy responsiveness, effects that may be related to a tumor cell's "TNF cytotoxicity threshold"[31]. Further support for this model comes from our finding that the subset of lung cancer patients whose tumors exhibited decreased *IRF6* expression in the setting of immunotherapy resistance also exhibited a strong EMT signature.

While it is unclear how Irf6 loss exerts its protective influence at a molecular level, a recent report in fish suggests that Irf6 can reduce the activity of IFN and NF-κB reporters in transfected 293T cells[50]. Future studies will be needed to understand how Irf6 regulates TNF cytotoxicity and to determine whether other pathways besides Irf6 and TNF signaling are dysregulated during EMT to contribute to acquired resistance.

Methods

Animals

C57BL/6, C57BL/6-Tg(TcraTcrb)1100Mjb/J (OT-I), and NOD/SCID mice were purchased from the Jackson Laboratory and/or bred at the University of Pennsylvania. Mice were housed under a 12h-12h light-dark cycle, temperature of 18–23°C, and pathogen-free conditions. All animal procedures used in this study were performed following the National Institutes of Health guidelines. All mouse procedure protocols used in this study were in accordance with, and with the approval of, the Institutional Animal Care and Use Committee (IACUC) of the University of Pennsylvania (protocols 804643 and 805650).

Cell lines

The 4662 murine PDAC cell line was derived from a spontaneous pancreatic cancer in a female KPC mouse on the C57BL/6J background as previously described[51]. 4662 early progressor ($n = 2$) and escape cell lines (E1 ~ 8, C7.e1, and C10.e1) were isolated from non-responders and recurrent tumors reaching ≥ 3 mm mean tumor diameter beyond day 75, respectively, following inoculation of the 4662 mouse PDAC cell line and treatment with chemoimmunotherapy or immunotherapy alone. Single cell clones were derived from the 4662 PDAC cell line by limiting dilution. 4662 PDAC cell lines with a full length of OVA and tdTomato as a surrogate have been generated as previously described[51]. PDAC cell lines were cultured in a standard cell culture medium including Dulbecco's Modified Eagle's medium (DMEM) with high glucose, 10% heat-inactivated FBS and Glutamax (GIBCO). These tumor cell lines were used for less than 20 passages and tested negative for mycoplasma contamination (MycoAlert Mycoplasma Detection Kit, Lonza). YFP labeling of cell lines was done with pCDH-CMV-EF1α-YFP, modified from pCDH-CMV-EF1α-RFP (System Biosciences, CD512B-1). We used 293T cells (Clontech, 632180) for lentivirus packaging.

Tumor implantation and therapy response assessment

5×10^5 4662 PDAC cells were implanted subcutaneously (s.c.) into 6-8-week-old female C57BL/6 mice and mice bearing PDAC were randomly allocated to each group and given therapy or control treatment. Some mice received 10^5 4662 PDAC cells in 50 µL DMEM orthotopically into the tail of pancreas on a sterile field under anesthesia. For tumor rechallenge, mice with complete response (CR) were administered control or T- or NK-cell depleting Ab and rested for 50 days, followed by subcutaneous inoculation of 10^6 4662 PDAC cells. For tumor growth kinetics, tumors were measured every 3–4 days by calipers and represented as the mean values of perpendicular diameters. For long-term survival studies, endpoint criteria included tumor volume exceeding 500 mm^3, severe cachexia, or weakness and inactivity, as per our mouse protocols. Tumors were harvested 18–21 days following implantation or a week after treatment for flow and tissue analyses. Therapy response assessment was defined as follows: Durable CR indicated the absence of palpable tumor at the completion of the experiment; CR with relapse indicated CR or near CR (≤ 1x1 mm tumor diameter) followed by progressive tumor growth; partial response denoted tumor regression to ≤ 30% of the maximum tumor diameter followed by progressive tumor growth; and finally, non-responders showed no response to therapy, transient stable disease, or limited response not meeting criteria for partial response.

In vivo treatment and T/NK-cell depletion

The general treatment schedule was previously described[17]. Briefly, mice with mean tumor diameter 5–7 mm (tumor volume around 100 mm^3) were enrolled and treated intraperitoneally (i.p.) with anti–PD-1 (clone RMP1-14, 200 µg/dose) for 7 times and anti–CTLA-4 (clone 9H10, 200 µg/dose) for 3 times every 3 days. Gemcitabine (Hospira) and nab-paclitaxel (Abraxane, Celgene) (120 mg/kg each), purchased from the Hospital of the University of Pennsylvania Pharmacy, were administered i.p. one time on the next

day of first ICB treatment. Anti-CD40 agonist (clone FGK45, 100 μg/dose) was co-injected i.p. with second dose of ICB. Control animals were treated with equivalent doses of isotype control antibodies.

Depletion of $CD4^+$ T cells, $CD8^+$ T cells, and NK cells was achieved by i.p. injections of anti-CD4 (clone GK1.5, 200 μg/dose), anti-CD8 (clone 2.43, 200 μg/dose), and anti-NK1.1 (clone PK136, 200 μg/dose) twice weekly from day 50 to 100, respectively. Control groups received isotype control antibodies. Depletions were confirmed by peripheral blood samples and end-of-study flow cytometry. All antibodies administered to mice were from Bio X Cell.

Adoptive transfer of tumor specific $CD8^+$ T cells

For adoptive transfer studies, 2×10^5 $OVA^{tdTomato}$-expressing 4662 parental and escape tumors were implanted s.c. into NOD/SCID mice. On day 14 when mean tumor diameter was 5–6 mm, 1.5×10^6 OVA-specific $CD8^+$ T cells prepared from spleen and lymph nodes of OT-I mice using mouse CD8α microbeads (Miltenyi Biotec, 130-117-044) and further flow cytometry sorting, followed by activation with immobilized 2 μg/ml of anti-CD3 (145-2C11; BioLegend) and 1 μg/ml of anti-CD28 (37.51; BioLegend) overnight, were transferred intravenously (i.v.) into tumor-bearing mice.

Flow cytometry of murine PDAC

For flow cytometric analyses, s.c. tumors were minced and digested in DMEM supplemented with 2 mg/ml of collagenase type IV (GIBCO, 17104-019) and 0.2 mg/ml of DNase I (Sigma, 10104159001) at 37℃ for 45 minutes and filtered through a 70-μM cell strainer to generate single cell suspensions. Cells were then stained with fluorescence-conjugated antibodies and a live/dead stain (Invitrogen, L34966) at 4℃ for 20 minutes and washed twice with cold PBS plus 5% FBS for sample acquisition. For intracellular caspase staining, cells were further permeabilized with Fix/Perm buffer (eBioscience, 00-5523-00) at 4℃ for 30 minutes and stained with active caspase-3 Ab (C92-605; BD Biosciences) in Perm buffer (eBioscience) at 4℃ for 30 minutes. Sample acquisition was performed by LSR II flow cytometry (BD Biosciences) and data were analyzed using FlowJo software (Tree Star). Gating strategies for immune cell populations were previously described[16] and shown in **Supplementary Fig. 1**. Antibodies used for flow cytometry are as follows: anti-mouse CD335 (NKp46) (29A1.4), CD103 (2E7), H-$2K^b$/H-$2D^b$ (28-8-6), H-$2K^b$ bound to SIINFEKL (25-D1.16), F4/80 (BM8), CD45 (30-F11), I-A/I-E (M5/114.15.2), CD11b (M1/70), Ly6C (HK1.4), Ly6G (1A8), CD11c (N418), CD3ε (145-2C11), CD8α (53 – 6.7), CD4 (RM4-5), CD25 (PC61), CD62L (MEL-14), CD44 (IM7; BD Biosciences), CD324 (E-cadherin) (DECMA-1), CD73 (TY/11.8), CD274 (PD-L1) (10F.9G2), CD155 (TX56). Antibodies were all from BioLegend unless otherwise indicated.

Lentiviral transduction of tumor cells for target gene modulation

The pCDH-EF1-FHC vector, a gift from Richard Wood (Addgene plasmid #64874), and pCDH-CMV-EF1α-YFP vector were used for constitutive overexpression. Full-length mouse *Zeb1* and *Snail* were gifts from Thomas Brabletz, University Erlangen, Germany. Murine *Irf6* gene was amplified based on the cDNA template from parental tumors. Point mutations in *Irf6* gene were performed using Q5 Site-Directed Mutagenesis Kit (NEB, E0552S) with mutagenic primers according to manufacturer's instructions and confirmed by sequencing.

The CRISPR vectors, lentiCRISPR v2 (a gift from Feng Zhang [Addgene plasmid #52961]) and LRG2.1 (a gift from Christopher Vakoc [Addgene plasmid #108098]), were used for target gene deletion. We further replaced GFP into YFP in the LRG2.1 vector. The sgRNA sequences were selected using a CRISPick tool (Broad Institue) and cloned into CRISPR vectors using a *BsmBI* restriction enzyme following the instruction from Addgene. CRISPR sgRNA sequences were listed in **Supplementary Table 2**.

Cloned plasmids were then co-transfected with pVSV-G (Addgene plasmid #8454) and psPAX2 (Addgene plasmid #12260) lentiviral packaging plasmids into 293T cells (Clontech) using polyethylenimine (PEI; Polysciences, 23966-100) in a ratio of 4:2:2 for plasmid DNA:pVSV-G:psPax2. Lentiviral particles were collected 72 hours after transfection and passed through a 0.45 μm PVDF filter for usage. Tumor cells were transduced with filtered viral supernatants in the presence of 8 μg/ml polybrene (Sigma, H9268) for 24 h, expanded for a couple of days, and selected with 8 μg/mL puromycin (Invitrogen, A1113803) for 5–7 d. YFP^+ cell sorting by flow cytometry was further conducted for double-gene modulation. Overexpression and knockout efficiencies were assessed by gene-specific qPCR analysis of target genes or western blotting.

Quantitative real-time PCR (qPCR)

RNA was isolated from cultured tumor cells using the NucleoSpin RNA Kit (Takara Bio) and reverse-transcribed by the High-capacity cDNA Reverse Transcription Kit (Life Technologies). Diluted cDNA was used for qPCR, which was performed with SsoAdvanced SYBR master mix (Bio-Rad) and the CFX384 Real-Time System (Bio-Rad). Results were normalized to *Tbp* expression using the Bio-Rad software. Primer sequences used for qPCR were in **Supplementary Table 2**.

Tumor and $CD8^+$ T cell co-culture

OVA-specific $CD8^+$ T cells from OT-I mice were sorted by CD8α MACS enrichment, followed by $CD3\varepsilon^+CD8\alpha^+$ cell sorting using flow cytometry, and maintained or activated overnight by pre-coated anti-CD3 (2 μg/ml) and anti-CD28 (1 μg/ml) in a RPMI 1640 culture medium supplemented with 10% FBS, 2.5% HEPES, 1% sodium pyruvate, 1% non-essential amino acids, 1% penicillin/streptomycin (Corning), and 0.1% 2-mercaptoenthanol (all from GIBCO unless otherwise indicated). Activated OT-I cells were co-cultured with $OVA^{tdTomato}$-transduced tumor cells at indicated ratios with or without 5 μg/ml of TNF-α neutralizing antibody (MP6-XT22; BioLegend), and two days later, T-cell killing was measured using

Annexin V Apoptosis Detection Kit (eBioscience, 88-8007-72) and 7-AAD Viability Staining Solution (BioLegend, 420404) according to the manufacturer's protocol by flow cytometry.

For T-cell priming assay, OVA-specific naïve CD3ε^{+}CD8α^{+}CD44^{lo}CD62L^{hi}CD25– T cells were sorted by flow cytometry, labelled with 5 μM CellTrace Violet (CTV; Invitrogen, C34557), and co-cultured with OVA^{tdTomato}-expressing tumor cells, treated with or without 100 ng/ml of IFN-γ (Peprotech, 315-05) overnight. Three days later, CTV dilution and CD44 and CD25 expression were analyzed on tdTomato^{-} CD8α^{+} gated OT-I cells by flow cytometry.

RNA-seq

RNA was prepared from tumor cells at steady states, 1 d after co-culture, and 2–3 weeks following implantation as described above. RNA-seq libraries were prepared either by Novogene (California, USA) or with the NEBNext Ultra II RNA Library Prep Kit (NEB, E7770S) according to the manufacturer's protocol. Libraries were then sequenced on Illumina next generation sequencers, generating either 150 bp paired end or 100 bp single end reads. Salmon v1.8.0[52] was used to generate raw counts in transcripts per million (TPM) through quasi-alignment to the mm39 reference genome using standard settings. The raw count matrix was subsequently imported into R-studio (R v4.1.2) for downstream normalization and differential gene expression analysis using DESeq2[53]. Genes were ranked by their Wald statistic for pre-ranked gene set enrichment analysis (GSEA)[54, 55]. Multiple published datasets were analyzed in the same manner. *De novo* and known motifs were identified within 500 bp of promoters of differentially expressed genes using HOMER's (v4.11) findMotifs.pl command[56].

ATAC-seq

Library construction – Libraries were prepared as previously described with minor modifications[57]. Briefly, concentrated Tn5 transposase (Diagenode) was diluted 10-fold using Tn5 dilution buffer (50mM Tris HCl pH 7.5, 100mM NaCl, 0.1mM EDTA, 1mM DTT, 0.1% NP-40, and 50% glycerol). Transposomes were assembled by loading the diluted Tn5 with the following Illumina sequencing adapters:

Read1 - TCGTCGGCAGCGTCAGATGTGTATAAGAGACAG

Read2 - /5Phos/GTCTCGTGGGCTCGGAGATGTGTATAAGAGACAG

Reverse - /5Phos/C*T*G*T*C*T*C*T*T*A*T*A*C*A*/3ddC/

Nuclei were isolated from 50,000 cells, followed immediately by transposition at 37^{o}C for 30 min. Transposed DNA fragments were purified using a Qiagen MinElute Kit, barcoded with primers based on Illumina TruSeq indices, and PCR amplified for 5 cycles using NEBNext High Fidelity 2x PCR master mix (NEB). Libraries were column-purified with the Qiagen PCR Cleanup kit, followed by 1.0x AMPure bead

cleanup. Library quality was assessed on 4200 TapeStation (Agilent), and concentrations were quantified by Qubit D1000 assay (ThermoFisher Scientific). Samples were sequenced using 150-cycle High Output NextSeq kits (Illumina, 20024907) to generate 75 bp paired end reads.

Analysis – Adapters were trimmed with Cutadapt v3.5 and reads were aligned to the mm39 mouse reference genome with Bowtie2 v2.4.4[58]. Sambamba v0.7.1[59] was used to filter out duplicates, while SAMtools v1.9[60] was used to identify and discard reads that aligned to the mitochondrial genome. Peaks were called with Genrich v0.6.1 (https://github.com/jsh58/Genrich) using standard settings in ATAC-seq mode and blacklisted regions were removed with BEDtools v2.30.0[61]. Overlapping peaks were identified with BEDtools, then merged. Raw read counts were determined with featureCounts v2.0.1[62], then imported into R Studio for normalization and differential analysis using DESeq2. Differentially accessible loci were annotated to genomic features using ChIPseeker[63]. Genes and enriched biological pathways associated with differentially accessible loci were determined by GREAT[64]. Motif discovery within differentially accessible loci was done with HOMER's findMotifsGenome.pl command.

Putative target promoters of transcription factors of interest were determined by overlapping mm39 promoters identified through ChIPseeker with known TF motifs. These target promoters were then intersected with the differentially accessible loci and annotated to their nearest genes using a mm39 annotations file and BEDOPS[65]. Genes were de-duplicated and their raw TPM counts were extracted from prior RNA-seq analysis. Genes were then filtered for fold changes of > = 2 or <=-2 and plotted by log2TPM.

For gene track visualization, scaled bigwig files were generated using deepTools v3.5.1[66]. Scaling factors were determined from edgeR's[67] calcNormFactors function using raw counts that were derived from featureCounts v2.0.1. Bigwig tracks were visualized using IGV's[68] genome browser and Gviz[69] in R Studio.

scRNA-seq analysis

Published raw single cell RNA-seq data derived from patient samples were analyzed using the 10x and Seurat v4 pipelines[70]. Briefly, raw counts were determined with Cell Ranger using the hg19 reference genome, and imported into R Studio for analysis using Seurat, as previously described. Data were initially filtered to include cells with at least 100 genes and all genes in at least 3 cells. Samples were merged and further filtered by mitochondrial read percentage and total transcripts. Samples were then integrated and normalized, and variable genes were determined. Cell subpopulations were clustered based on the expression of certain gene markers. The epithelial cell cluster was further subsetted by the mean expression level of certain genes of interest, and the top differentially expressed genes were identified in the high (> mean) and low (< mean) subsets. These differentially expressed genes were used as gene sets for downstream GSEA.

Immunofluorescence and Hematoxylin & Eosin (H&E) staining

Tissues were fixed in Zinc-formalin and embedded in paraffin for histological analysis and immunofluorescence (IF) staining. For IF staining, sections were deparaffinized, rehydrated, and prepared by antigen retrieval. They were then blocked in PBS with 0.3% Triton-X and 5% donkey serum for 1 hour, stained with primary and secondary antibodies, and mounted with Aqua Polymount (Polysciences). Primary antibodies used include chicken anti-GFP (Abcam, ab13970) and rabbit anti-cleaved caspase-3 (Cell Signaling Technology, 9661). Slides were visualized using an Olympus IX71 inverted multicolor fluorescent microscope equipped with a DP71 camera. ImageJ FIJI software was used for quantification, with each data point an average of 2–3 fields per tumor section.

For H&E staining, sections were deparaffinized, rehydrated, stained with hematoxylin, differentiated with acidic ethanol, stained for eosin, dehydrated, and mounted with Permount. Slides were visualized using an Olympus BX41 microscope equipped with a DP25 camera.

Cell proliferation and viability assay

For checking cell proliferation, 10^4 tumor cells were seeded in each 12-well in triplicates and cell density at indicated time points was measured by staining with Hoechst 33342 Solution (Thermo Scientific, 62249) and detecting by spectrometry. Data were normalized to background control and calculated by percent of cell growth compared to day 0.

Cell viability in response to TNF was determined as previously described[42] with some modification. Briefly, $3–5\times10^3$ tumor cells were plated in a 96-well plate and treated with 0.2 μg/ml of IFN-γ (Peprotech, 315-05) plus 1 μg/ml of cycloheximide (Cell Signaling Technology, 2112S) and indicated concentrations of TNF-α (BioLegend, 575204). A pan-caspase inhibitor, Z-VAD-FMK, was purchased from Selleckchem (S7023). Two days later, cell viability was measured by CellTiter-Glo (Promega, G7571) according to manufacturer's instructions. Data were normalized to each group without TNF treatment and a group with the lowest viability. IC_{50} and nonlinear regression curve fits by log(inhibitor) vs. normalized response test were determined using GraphPad Prism 9 (GraphPad).

Immunoblot analysis

Tumor cells with or without TNF-α treatment or genetic modification were lysed in RIPA lysis buffer with protease and phosphatase inhibitor cocktail (Thermo Scientific, 78444). Equivalent amounts of protein from whole cell lysates were separated by SDS-PAGE and transferred onto PVDF membranes (Bio-Rad). Membranes were blocked in 5% nonfat milk in PBS plus 0.1% Tween-20 and stained with primary antibodies, followed by probing with horseradish peroxidase-conjugated secondary antibodies (Jackson Immunoresearch). Primary antibodies used include goat anti-IRF6 (Novus Biologicals, NBP1-51911), rabbit anti-TRADD (Cell Signaling Technology, 3694), mouse anti-FADD (1F7; Enzo Life Sciences, ADI-

AAM-212-E), rabbit anti-Caspase-8 (D35G2; Cell Signaling Technology, 4790), rabbit anti-IκBα (Cell Signaling Technology, 9242), rabbit anti-phospho-NF-κB p65 (Ser536) (Cell Signaling Technology, 3031), rabbit anti-NF-κB p65 (D14E12; Cell Signaling Technology, 8242), and rabbit anti-GAPDH (14C10; Cell Signaling Technology, 2118). ECL solution (Thermo Scientific, 32106) was used as a substrate and band signals were detected using ChemiDoc (Bio-Rad).

Software, statistics, and reproducibility

PRISM and R were used for data processing, statistical analysis, and data visualization. The R language and environment for graphics (https://www.r-project.org) was used in this study for the bioinformatics analysis of RNA-seq and ATAC-seq data. The R packages used for all analysis described in this manuscript were from the Bioconductor and CRAN. Statistical comparisons between two groups were performed using unpaired two-tailed Student's *t* test. For comparisons between multiple groups, one-way ANOVA with Tukey's HSD post-test was used. For survival comparison between two groups, log-rank (Mantel-Cox) *P* values of Kaplan-Meier curves were determined using GraphPad Prism 9 (GraphPad). On graphs, bars represent either range or standard error of mean (SEM). For all figures, $P < 0.05$ was considered statistically significant, * indicates $P < 0.05$, ** $P < 0.01$, and *** $P < 0.0001$. No statistical method was used to pre-determine the sample size, which was chosen on the basis of previous experimental experience. No data were excluded from the analyses. For measuring tumor phenotypes *in vivo*, investigators were not blinded to group information, however, the results were reproducible by two independent researchers in different animal facilities. For *in vitro* experiments, blinding was not required because all the samples were analyzed in a consistent manner.

Declarations

Data availability

The RNA-seq and ATAC-seq data generated in this study are available in the NCBI Gene Expression Omnibus (GEO) under accession numbers GSE222223 and GSE222224.

Code availability

All the code used in this study will be available upon request, including RNA-seq and ATAC-seq analyses.

Acknowledgements

We thank members of the Stanger and Vonderheide laboratories, as well as the Penn Pancreatic Cancer Research Center, for technical help and scientific discussions. This work was supported by a grant from the NIH (CA229803), the Abramson Family Cancer Research Institute, the Abramson Cancer Center, and the NIH/Penn Center for Molecular Studies in Digestive and Liver Diseases (P30DK050306).

Author contributions

M.S.D., R.H.V., and B.Z.S. conceived the project. I.K., M.S.D., S.Y., R.H.V., and B.Z.S. designed the study. I.K., M.S.D., S.Y., S.B.K., Q.L., J.H.L., J.L., R.J.N., S.K.T., and M.M performed experiments, analyzed data, and discussed for this study. S.Y. and J. W. T. performed bioinformatics analysis. T.K. and K.P. provided experimental and human data resources. I.K., M.S.D., S.Y., R.H.V., and B.Z.S. wrote and revised the manuscript. B.Z.S. and R.H.V. supervised this study. All authors discussed the findings and provided input on the manuscript.

Competing interests

Dr. Stanger receives research funding from Boehringer-Ingelheim and previously served as a consultant to iTeos Therapeutics. Dr. Vonderheide reports receiving consulting fees from BMS, is an inventor on a licensed patents relating to cancer cellular immunotherapy and cancer vaccines and receives royalties from Children's Hospital Boston for a licensed research-only monoclonal antibody.

Correspondence and requests for materials should be addressed to Robert H. Vonderheide or Ben Z. Stanger.

References

1. Ribas, A. & Wolchok, J.D. Cancer immunotherapy using checkpoint blockade. *Science* **359**, 1350-1355 (2018).
2. Sharma, P. *et al.* The Next Decade of Immune Checkpoint Therapy. *Cancer discovery* **11**, 838-857 (2021).
3. Schachter, J. *et al.* Pembrolizumab versus ipilimumab for advanced melanoma: final overall survival results of a multicentre, randomised, open-label phase 3 study (KEYNOTE-006). *Lancet* **390**, 1853-1862 (2017).
4. Doroshow, D.B. *et al.* Immunotherapy in Non-Small Cell Lung Cancer: Facts and Hopes. *Clinical cancer research : an official journal of the American Association for Cancer Research* **25**, 4592-4602 (2019).
5. Yuan, S., Norgard, R.J. & Stanger, B.Z. Cellular Plasticity in Cancer. *Cancer Discov* **9**, 837-851 (2019).
6. Dongre, A. & Weinberg, R.A. New insights into the mechanisms of epithelial-mesenchymal transition and implications for cancer. *Nature reviews. Molecular cell biology* **20**, 69-84 (2019).
7. Yang, J. *et al.* Guidelines and definitions for research on epithelial-mesenchymal transition. *Nature reviews. Molecular cell biology* **21**, 341-352 (2020).
8. Chen, L. *et al.* Metastasis is regulated via microRNA-200/ZEB1 axis control of tumour cell PD-L1 expression and intratumoral immunosuppression. *Nature communications* **5**, 5241 (2014).
9. Dongre, A. *et al.* Epithelial-to-Mesenchymal Transition Contributes to Immunosuppression in Breast Carcinomas. *Cancer research* **77**, 3982-3989 (2017).
10. Kudo-Saito, C., Shirako, H., Takeuchi, T. & Kawakami, Y. Cancer metastasis is accelerated through immunosuppression during Snail-induced EMT of cancer cells. *Cancer cell* **15**, 195-206 (2009).

11. Terry, S. *et al.* New insights into the role of EMT in tumor immune escape. *Molecular oncology* **11**, 824-846 (2017).
12. Dongre, A. *et al.* Direct and Indirect Regulators of Epithelial-Mesenchymal Transition-Mediated Immunosuppression in Breast Carcinomas. *Cancer discovery* **11**, 1286-1305 (2021).
13. O'Hara, M.H. *et al.* CD40 agonistic monoclonal antibody APX005M (sotigalimab) and chemotherapy, with or without nivolumab, for the treatment of metastatic pancreatic adenocarcinoma: an open-label, multicentre, phase 1b study. *The Lancet. Oncology* **22**, 118-131 (2021).
14. Padron, L.J. *et al.* Sotigalimab and/or nivolumab with chemotherapy in first-line metastatic pancreatic cancer: clinical and immunologic analyses from the randomized phase 2 PRINCE trial. *Nature medicine* **28**, 1167-1177 (2022).
15. Byrne, K.T. & Vonderheide, R.H. CD40 Stimulation Obviates Innate Sensors and Drives T Cell Immunity in Cancer. *Cell reports* **15**, 2719-2732 (2016).
16. Li, J. *et al.* Tumor Cell-Intrinsic Factors Underlie Heterogeneity of Immune Cell Infiltration and Response to Immunotherapy. *Immunity* **49**, 178-193 e177 (2018).
17. Winograd, R. *et al.* Induction of T-cell Immunity Overcomes Complete Resistance to PD-1 and CTLA-4 Blockade and Improves Survival in Pancreatic Carcinoma. *Cancer immunology research* **3**, 399-411 (2015).
18. Morrison, A.H., Diamond, M.S., Hay, C.A., Byrne, K.T. & Vonderheide, R.H. Sufficiency of CD40 activation and immune checkpoint blockade for T cell priming and tumor immunity. *Proceedings of the National Academy of Sciences of the United States of America* **117**, 8022-8031 (2020).
19. Singh, A. & Settleman, J. EMT, cancer stem cells and drug resistance: an emerging axis of evil in the war on cancer. *Oncogene* **29**, 4741-4751 (2010).
20. Hegde, S. *et al.* Dendritic Cell Paucity Leads to Dysfunctional Immune Surveillance in Pancreatic Cancer. *Cancer cell* **37**, 289-307 e289 (2020).
21. Lin, J.H. *et al.* Type 1 conventional dendritic cells are systemically dysregulated early in pancreatic carcinogenesis. *The Journal of experimental medicine* **217** (2020).
22. Kemp, S.B. *et al.* Efficacy of a small molecule inhibitor of KrasG12D in immunocompetent models of pancreatic cancer. *Cancer discovery* (2022).
23. Li, F. *et al.* The association between CD8+ tumor-infiltrating lymphocytes and the clinical outcome of cancer immunotherapy: A systematic review and meta-analysis. *EClinicalMedicine* **41**, 101134 (2021).
24. Zhang, L. *et al.* Intratumoral T cells, recurrence, and survival in epithelial ovarian cancer. *The New England journal of medicine* **348**, 203-213 (2003).
25. Elyada, E. *et al.* Cross-Species Single-Cell Analysis of Pancreatic Ductal Adenocarcinoma Reveals Antigen-Presenting Cancer-Associated Fibroblasts. *Cancer discovery* **9**, 1102-1123 (2019).
26. Lee, J.J. *et al.* Elucidation of Tumor-Stromal Heterogeneity and the Ligand-Receptor Interactome by Single-Cell Transcriptomics in Real-world Pancreatic Cancer Biopsies. *Clinical cancer research : an*

official journal of the American Association for Cancer Research **27**, 5912-5921 (2021).

27. Steele, N.G. *et al.* Multimodal Mapping of the Tumor and Peripheral Blood Immune Landscape in Human Pancreatic Cancer. *Nature cancer* **1**, 1097-1112 (2020).
28. Gettinger, S. *et al.* Impaired HLA Class I Antigen Processing and Presentation as a Mechanism of Acquired Resistance to Immune Checkpoint Inhibitors in Lung Cancer. *Cancer discovery* **7**, 1420-1435 (2017).
29. Webster, J.D. & Vucic, D. The Balance of TNF Mediated Pathways Regulates Inflammatory Cell Death Signaling in Healthy and Diseased Tissues. *Frontiers in cell and developmental biology* **8**, 365 (2020).
30. Kearney, C.J. *et al.* Tumor immune evasion arises through loss of TNF sensitivity. *Science immunology* **3** (2018).
31. Vredevoogd, D.W. *et al.* Augmenting Immunotherapy Impact by Lowering Tumor TNF Cytotoxicity Threshold. *Cell* **178**, 585-599 e515 (2019).
32. Kondo, S. *et al.* Mutations in IRF6 cause Van der Woude and popliteal pterygium syndromes. *Nature genetics* **32**, 285-289 (2002).
33. Jerby-Arnon, L. *et al.* A Cancer Cell Program Promotes T Cell Exclusion and Resistance to Checkpoint Blockade. *Cell* **175**, 984-997 e924 (2018).
34. Auslander, N. *et al.* Robust prediction of response to immune checkpoint blockade therapy in metastatic melanoma. *Nature medicine* **24**, 1545-1549 (2018).
35. Jiang, P. *et al.* Signatures of T cell dysfunction and exclusion predict cancer immunotherapy response. *Nature medicine* **24**, 1550-1558 (2018).
36. Schoenfeld, A.J. & Hellmann, M.D. Acquired Resistance to Immune Checkpoint Inhibitors. *Cancer cell* **37**, 443-455 (2020).
37. Beatty, G.L. *et al.* CD40 agonists alter tumor stroma and show efficacy against pancreatic carcinoma in mice and humans. *Science* **331**, 1612-1616 (2011).
38. Sharma, P., Hu-Lieskovan, S., Wargo, J.A. & Ribas, A. Primary, Adaptive, and Acquired Resistance to Cancer Immunotherapy. *Cell* **168**, 707-723 (2017).
39. Shields, B.D. *et al.* Indicators of responsiveness to immune checkpoint inhibitors. *Scientific reports* **7**, 807 (2017).
40. Thompson, J.C. *et al.* Gene signatures of tumor inflammation and epithelial-to-mesenchymal transition (EMT) predict responses to immune checkpoint blockade in lung cancer with high accuracy. *Lung cancer* **139**, 1-8 (2020).
41. Wang, G. *et al.* The pan-cancer landscape of crosstalk between epithelial-mesenchymal transition and immune evasion relevant to prognosis and immunotherapy response. *NPJ precision oncology* **5**, 56 (2021).
42. Cucolo, L. *et al.* The interferon-stimulated gene RIPK1 regulates cancer cell intrinsic and extrinsic resistance to immune checkpoint blockade. *Immunity* **55**, 671-685 e610 (2022).

43. Kearney, C.J. *et al.* PD-L1 and IAPs co-operate to protect tumors from cytotoxic lymphocyte-derived TNF. *Cell death and differentiation* **24**, 1705-1716 (2017).
44. Roehle, K. *et al.* cIAP1/2 antagonism eliminates MHC class I-negative tumors through T cell-dependent reprogramming of mononuclear phagocytes. *Science translational medicine* **13** (2021).
45. Lee, Y.G. *et al.* Modulation of BCL-2 in Both T Cells and Tumor Cells to Enhance Chimeric Antigen Receptor T-cell Immunotherapy against Cancer. *Cancer discovery* **12**, 2372-2391 (2022).
46. Vander Velde, R., Shaffer, S. & Marusyk, A. Integrating mutational and nonmutational mechanisms of acquired therapy resistance within the Darwinian paradigm. *Trends in cancer* **8**, 456-466 (2022).
47. Savitsky, D., Tamura, T., Yanai, H. & Taniguchi, T. Regulation of immunity and oncogenesis by the IRF transcription factor family. *Cancer immunology, immunotherapy : CII* **59**, 489-510 (2010).
48. Botti, E. *et al.* Developmental factor IRF6 exhibits tumor suppressor activity in squamous cell carcinomas. *Proceedings of the National Academy of Sciences of the United States of America* **108**, 13710-13715 (2011).
49. Alade, A.A. *et al.* Non-random distribution of deleterious mutations in the DNA and protein-binding domains of IRF6 are associated with Van Der Woude syndrome. *Molecular genetics & genomic medicine* **8**, e1355 (2020).
50. Liang, Y. *et al.* Negative regulation of interferon regulatory factor 6 (IRF6) in interferon and NF-kappaB signalling pathways of common carp (Cyprinus carpio L.). *BMC veterinary research* **18**, 433 (2022).
51. Evans, R.A. *et al.* Lack of immunoediting in murine pancreatic cancer reversed with neoantigen. *JCI insight* **1** (2016).
52. Dobin, A. *et al.* STAR: ultrafast universal RNA-seq aligner. *Bioinformatics* **29**, 15-21 (2013).
53. Love, M.I., Huber, W. & Anders, S. Moderated estimation of fold change and dispersion for RNA-seq data with DESeq2. *Genome biology* **15**, 550 (2014).
54. Mootha, V.K. *et al.* PGC-1alpha-responsive genes involved in oxidative phosphorylation are coordinately downregulated in human diabetes. *Nature genetics* **34**, 267-273 (2003).
55. Subramanian, A. *et al.* Gene set enrichment analysis: a knowledge-based approach for interpreting genome-wide expression profiles. *Proceedings of the National Academy of Sciences of the United States of America* **102**, 15545-15550 (2005).
56. Heinz, S. *et al.* Simple combinations of lineage-determining transcription factors prime cis-regulatory elements required for macrophage and B cell identities. *Molecular cell* **38**, 576-589 (2010).
57. Buenrostro, J.D., Giresi, P.G., Zaba, L.C., Chang, H.Y. & Greenleaf, W.J. Transposition of native chromatin for fast and sensitive epigenomic profiling of open chromatin, DNA-binding proteins and nucleosome position. *Nature methods* **10**, 1213-1218 (2013).
58. Langmead, B. & Salzberg, S.L. Fast gapped-read alignment with Bowtie 2. *Nature methods* **9**, 357-359 (2012).

59. Tarasov, A., Vilella, A.J., Cuppen, E., Nijman, I.J. & Prins, P. Sambamba: fast processing of NGS alignment formats. *Bioinformatics* **31**, 2032-2034 (2015).
60. Li, H. *et al.* The Sequence Alignment/Map format and SAMtools. *Bioinformatics* **25**, 2078-2079 (2009).
61. Quinlan, A.R. & Hall, I.M. BEDTools: a flexible suite of utilities for comparing genomic features. *Bioinformatics* **26**, 841-842 (2010).
62. Liao, Y., Smyth, G.K. & Shi, W. featureCounts: an efficient general purpose program for assigning sequence reads to genomic features. *Bioinformatics* **30**, 923-930 (2014).
63. Yu, G., Wang, L.G. & He, Q.Y. ChIPseeker: an R/Bioconductor package for ChIP peak annotation, comparison and visualization. *Bioinformatics* **31**, 2382-2383 (2015).
64. McLean, C.Y. *et al.* GREAT improves functional interpretation of cis-regulatory regions. *Nature biotechnology* **28**, 495-501 (2010).
65. Neph, S. *et al.* BEDOPS: high-performance genomic feature operations. *Bioinformatics* **28**, 1919-1920 (2012).
66. Ramirez, F. *et al.* deepTools2: a next generation web server for deep-sequencing data analysis. *Nucleic acids research* **44**, W160-165 (2016).
67. Robinson, M.D., McCarthy, D.J. & Smyth, G.K. edgeR: a Bioconductor package for differential expression analysis of digital gene expression data. *Bioinformatics* **26**, 139-140 (2010).
68. Robinson, J.T. *et al.* Integrative genomics viewer. *Nature biotechnology* **29**, 24-26 (2011).
69. Hahne, F. & Ivanek, R. Visualizing Genomic Data Using Gviz and Bioconductor. *Methods in molecular biology* **1418**, 335-351 (2016).
70. Hao, Y. *et al.* Integrated analysis of multimodal single-cell data. *Cell* **184**, 3573-3587 e3529 (2021).

Figures

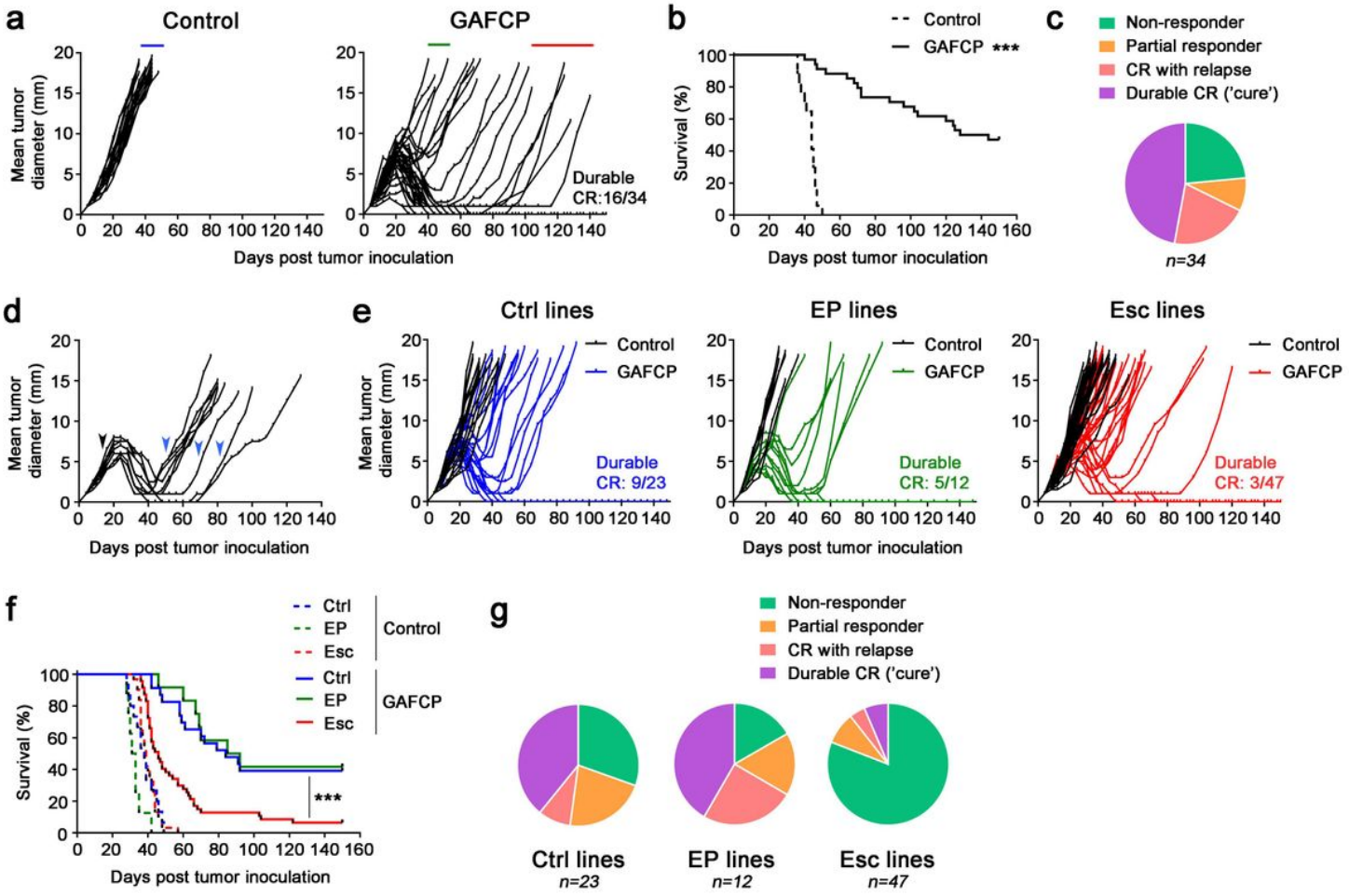

Figure 1

Recurrent PDAC develops acquired resistance to combination therapy. a,**b**, Mice were injected subcutaneously (s.c.) with 4662 PDAC cells and treated intraperitoneally (i.p.) with control IgG (*n* = 17) or chemoimmunotherapy (*n*= 34) consisting of gemcitabine (G), nab-paclitaxel (A), αCD40 agonistic Ab (F), and checkpoint blockades αCTLA-4 (C) and αPD-1 (P) Abs. Tumor growth (**a**) and survival (**b**) were monitored. **c**, The proportion of non-responders and mice with partial response (PR), relapsed after complete response (CR), and durable CR upon treatment was depicted. **d**, Mice with recurrent tumors after CR or near CR were re-treated with GFCP (blue arrows) and tumor sizes were measured. **e**–**g**, Tumor cell lines were generated from s.c. tumors with control IgG ('Ctrl' lines, *n* = 4), early progressor ('EP' lines, *n* = 2), and the relapsed after CR ('Esc' lines, *n* = 8) upon therapy, as denoted by blue, green, and red lines in **a**, respectively. Naïve WT mice challenged s.c. with these cell lines were treated with control IgG (*n* = 3 or 4 per line) or GAFCP (*n* = 5 or 6 per line) and tumor growth (**e**) and survival (**f**) were monitored. Response rates (**g**) in mice received each cell line followed by treatment are shown.

Figure 2

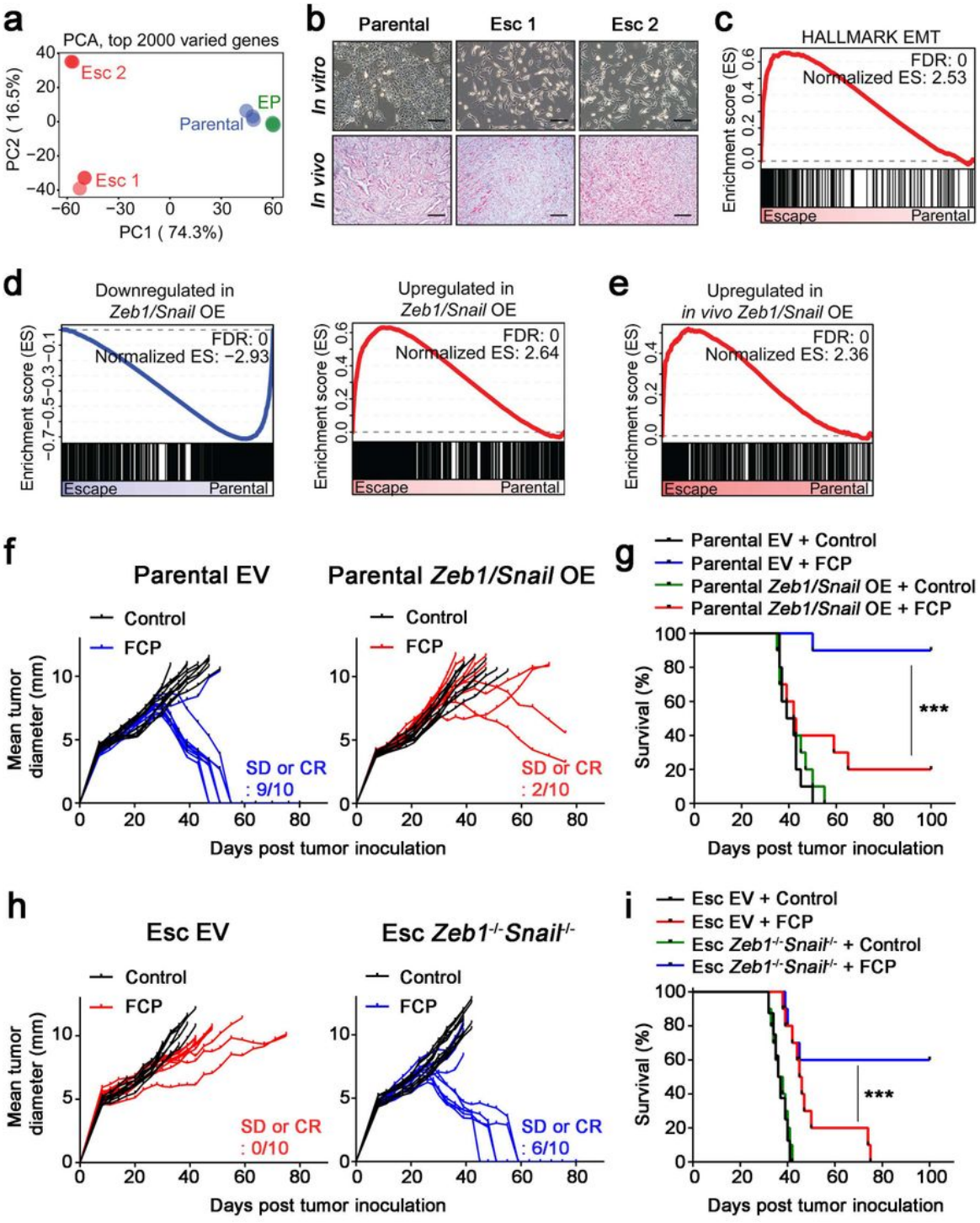

Figure 2

EMT induces immunotherapy resistance in PDAC. a, Principal component analysis (PCA) plot of RNA-seq data from parental, EP, and Esc cell lines (triplicates) is depicted. **b**, Representative bright field (top) and H&E (bottom) images of cell lines and s.c. implanted tumors on day 18, respectively. Scale bars, 250 μm. **c**, GSEA of the EMT Hallmark (Molecular Signature Database) in 4662 parental vs. Esc cell lines. Normalized enrichment score (NES) and false discovery rate (FDR) are shown. **d**, GSEA plots of gene

signatures derived from 4662 parental cells overexpressing *Zeb1* and *Snail* (*Zeb1*/*Snail* OE) in 4662 parental vs. Esc lines. Gene signatures downregulated (left) and upregulated (right) with *Zeb1*/*Snail* OE are shown. **e**, GSEA plot of a gene signature derived from s.c. implanted *Zeb1*/*Snail* OE tumors in s.c. implanted parental vs. Esc tumors. **f**,**g**, Individual tumor growth (**f**) and survival (**g**) of mice bearing s.c. implanted 4662 parental empty vector (EV, left) and *Zeb1*/*Snail* OE (right) tumors treated with either control IgG or FCP (n = 10). **h**,**i**, Individual tumor growth (**h**) and survival (**i**) of mice bearing s.c. implanted 4662 Esc EV (left) and $Zeb1^{-/-}Snail^{-/-}$ (right) tumors treated with either control IgG or FCP (n = 10). SD, stable disease. Clonal 4662 (C7 and C10) and derived Esc (C7.e1 and C10.e1) lines were used for genetic modification, and both lines showed a similar phenotype. Data represent two independent experiments.

Figure 3

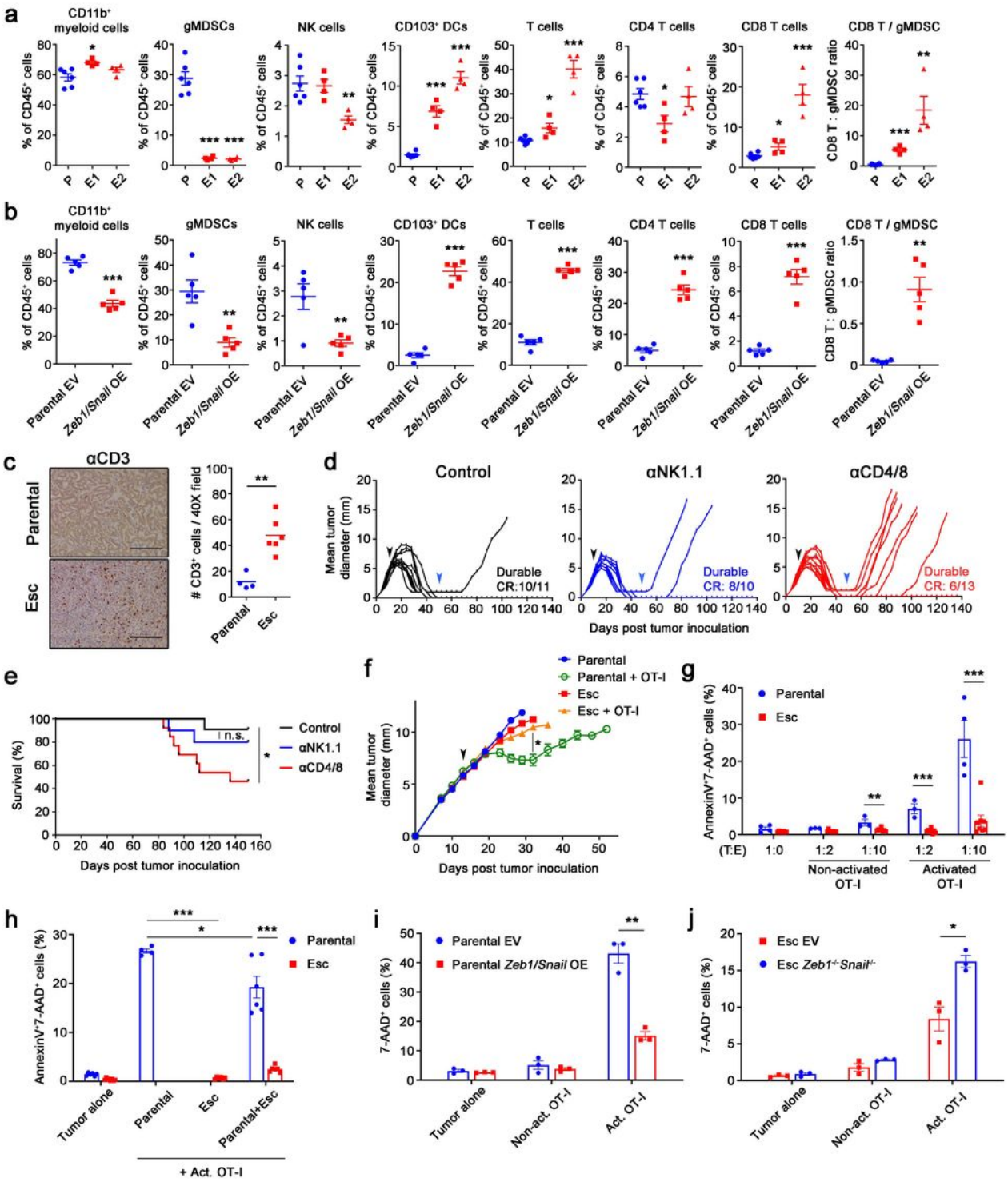

Figure 3

EMT mediates cell-autonomous resistance to direct cytolytic T cell killing. a,**b**, Flow cytometric analysis of immune populations in s.c. implanted 4662 parental (P, *n* = 6) vs. Esc (E1 and E2, *n* = 4 per line) (**a**) and 4662 parental EV (*n* = 5) vs. *Zeb1/Snail* OE (*n* = 5) tumors (**b**) on day 18 post inoculation. **c**, Representative αCD3 IHC images (left) and quantitation (right) from s.c. implanted parental and Esc tumors (*n* = 4 or 6). Scale bars, 250 μm. **d**,**e**, Mice with CR or near CR after therapy (black arrows) were

treated with control IgG (n = 11), depleting αNK1.1 Ab (n = 10), or αCD4 and αCD8 Abs (n = 13), starting from day 50 (blue arrows) post tumor inoculation, and monitored for tumor recurrence (**d**). The corresponding survival curves are shown in **e**. n.s., non-significant. **f**, Tumor growth of s.c. inoculated OVA-transduced 4662 parental and Esc tumors in NOD/SCID mice, with or without adoptive transfer of activated OVA-specific $CD8^+$ T cells (OT-I) on day 14 (arrow). **g**, OVA-tdTomato$^+$ 4662 parental and Esc tumors were co-cultured with non-activated or activated OT-I by αCD3 and αCD28 Abs overnight, at indicated tumor to effector (T:E) ratios. Two days later, AnnexinV and 7-AAD expression on tumor cells were determined by flow cytometry. **h**, OVA^+ 4662 parental and Esc tumors were additionally transduced with each fluorescence YFP or CFP, plated separately or mixed, and co-cultured with activated OT-I. AnnexinV and 7-AAD on each tumor were measured 2 d after co-culture. **i**,**j**, The percentages of 7-AAD$^+$ cells on co-cultured OVA^+ 4662 parental EV vs. *Zeb1*/*Snail* OE tumors (**i**) and 4662 Esc EV vs. *Zeb1*$^{-/-}$ *Snail*$^{-/-}$ tumors (**j**) with or without OT-I for 2 d. Data represent two independent experiments.

Figure 4

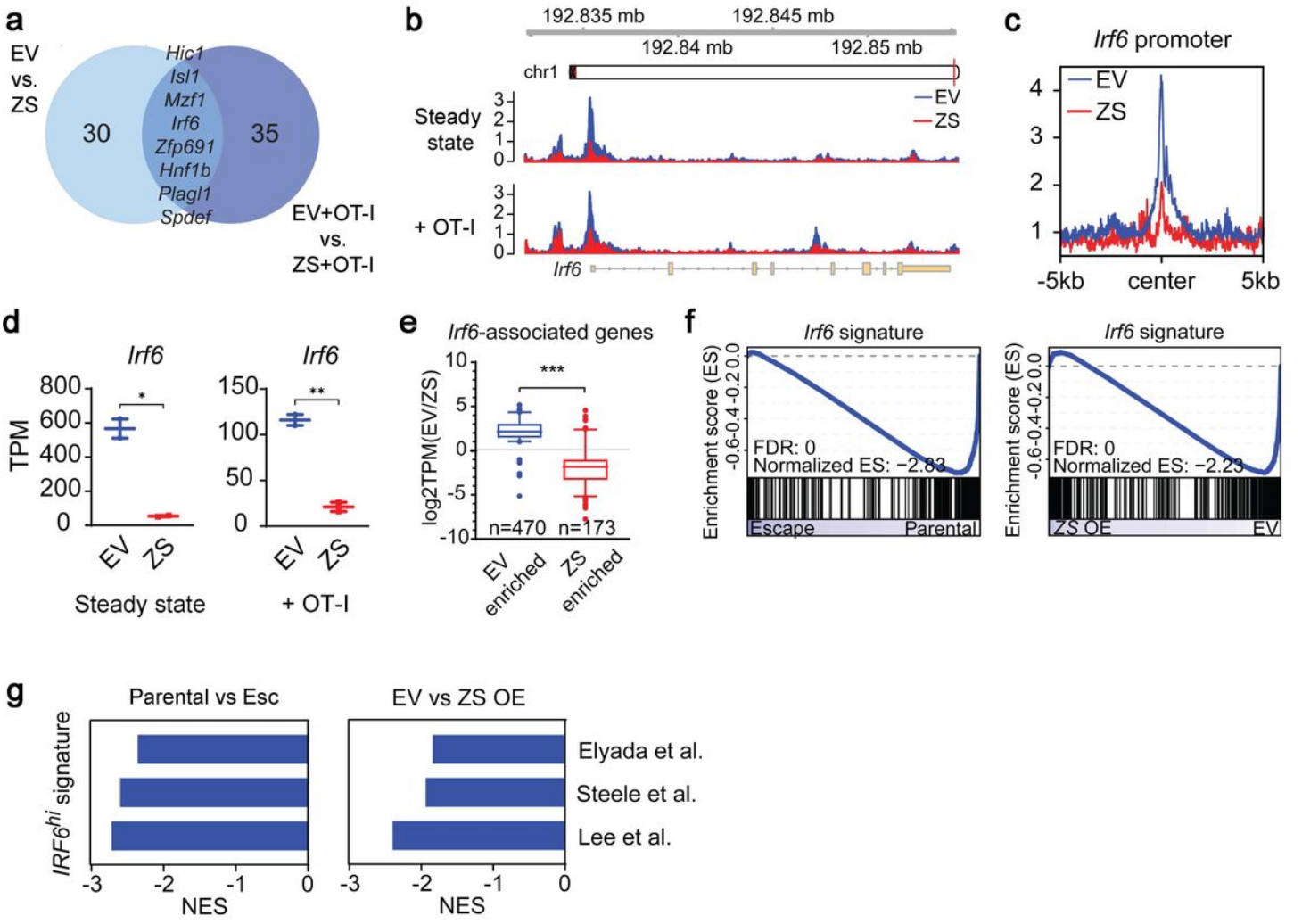

Figure 4

Transcriptional and chromatin profiling identifies Irf6as a potential regulator of acquired immunotherapy resistance. a, Venn diagram of HOMER *de novo* motifs identified in chromatin regions significantly enriched in EV vs. *Zeb1/Snail* OE (ZS) cell lines that have (right) or have not (left) been co-cultured with OT-1 cells. Significantly enriched chromatin regions were defined as |log2fold change| > 1.4 and p-value < 0.05 after DESeq2 analysis. **b**, Genome browser track showing ATAC-seq reads along the *Irf6* gene. **c**, Aggregate plots comparing the average ATAC signal of EV (blue) and *Zeb1/Snail* OE (red) tumors around all putative *Irf6* promoter sequences. More details are described in the **Methods section**. **d**, Transcripts per million (TPMs) of *Irf6* in EV vs. *Zeb1/Snail*OE tumors that have (right) or have not (left) been co-cultured with OT-1 cells. Each dot represents biological replicates. **e**, Boxplots of log2fold changes in the expression of *Irf6*-associated genes with differentially open chromatin in parental EV (left, n=470 genes) vs. *Zeb1/Snail* OE (right, n=173 genes) tumors. **f**, GSEA plots of an *Irf6*-dependent gene signature (derived by comparing *Irf6*-expressing tumors to controls) in parental vs. Esc (left) and parental EV vs. *Zeb1/Snail* OE (right) tumors. **g**, GSEA of gene signatures derived from human PDAC cells that highly express *IRF6* in parental vs. Esc (left) and EV vs *Zeb1/Snail* OE tumors (right). Negative normalized enrichment scores (NES) demonstrate enrichment in parental and EV tumors compared to Esc and *Zeb1/Snail* OE tumors, respectively.

Figure 5

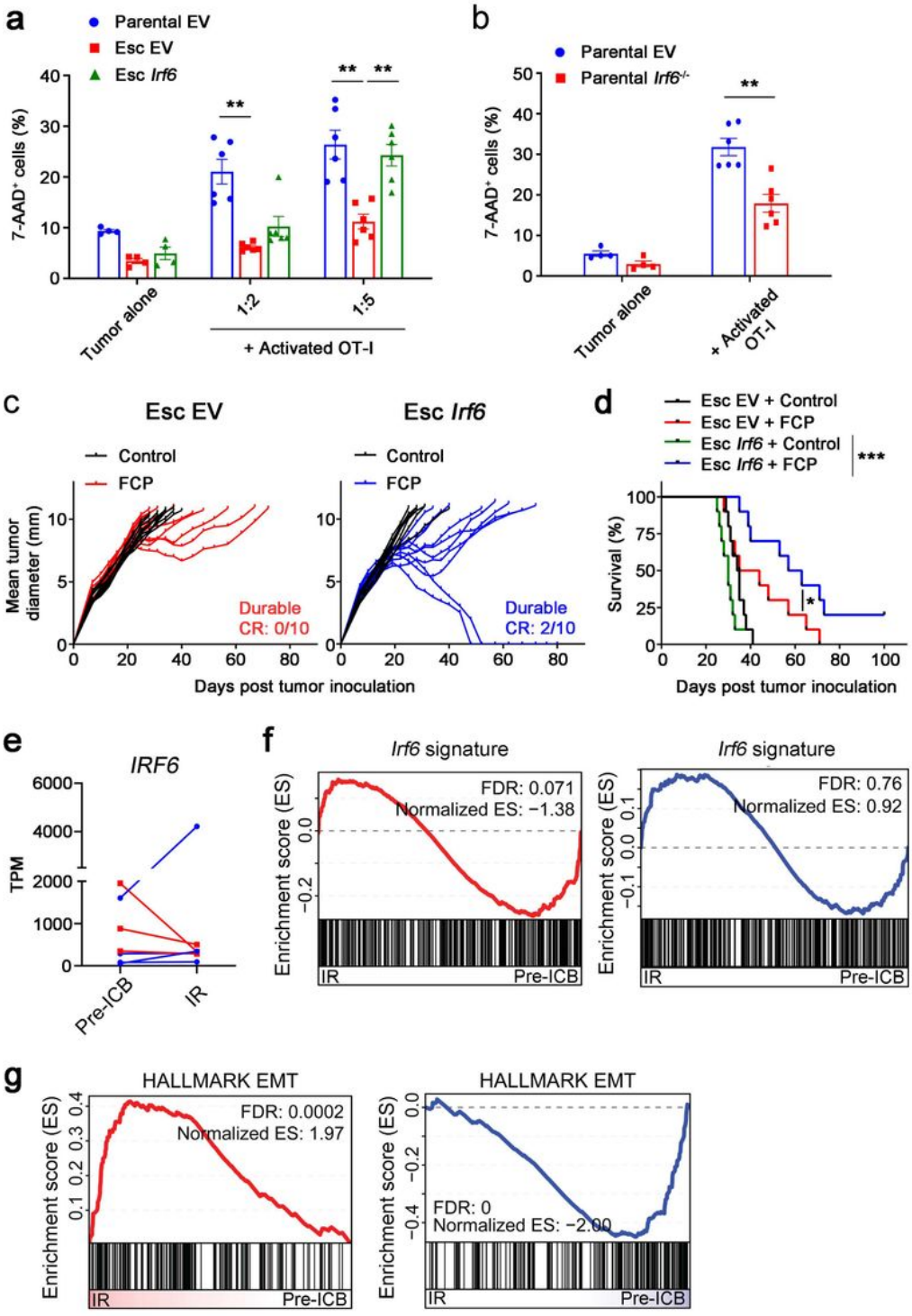

Figure 5

Irf6 loss contributes to EMT-induced immunotherapy resistance. a, OVA-tdTomato$^+$ 4662 parental EV, Esc EV, and Esc *Irf6* tumors were co-cultured with or without activated OT-I at indicated 4662 tumors to OT-I ratios for 2 d. 7-AAD expression on tumors was measured by flow cytometry. **b**, OVA-tdTomato$^+$ 4662 parental EV and *Irf6* KO tumors were used as target cells (1:5 ratio). **c**,**d**, Tumor growth (**c**) and survival (**d**) of mice bearing 4662 Esc EV and Esc *Irf6* tumors treated with control IgG or FCP (n = 10). Data represent

two independent experiments. **e**, TPMs of *IRF6* in 7 treatment-paired NSCLC patient samples (Gettinger et al., 2017). All patients demonstrated initial response to combinatorial checkpoint blockade before relapsing. Lines are drawn from patient-matched early treatment (Pre-ICB) to immunotherapy recurrence (IR). Red lines indicate 3 patient samples demonstrating a decrease in *IRF6* expression with recurrence. Blue lines indicate the others demonstrating unchanged or increased *IRF6* expression with recurrence. **f**,**g**, GSEA plots of an *Irf6*-dependent gene signature derived from *Irf6*-expressing 4662 tumors (**f**) and the EMT Hallmark (**g**) in patient-matched Pre-ICB vs. IR samples separately assorted based on *IRF6* expression as in **e**.

Figure 6

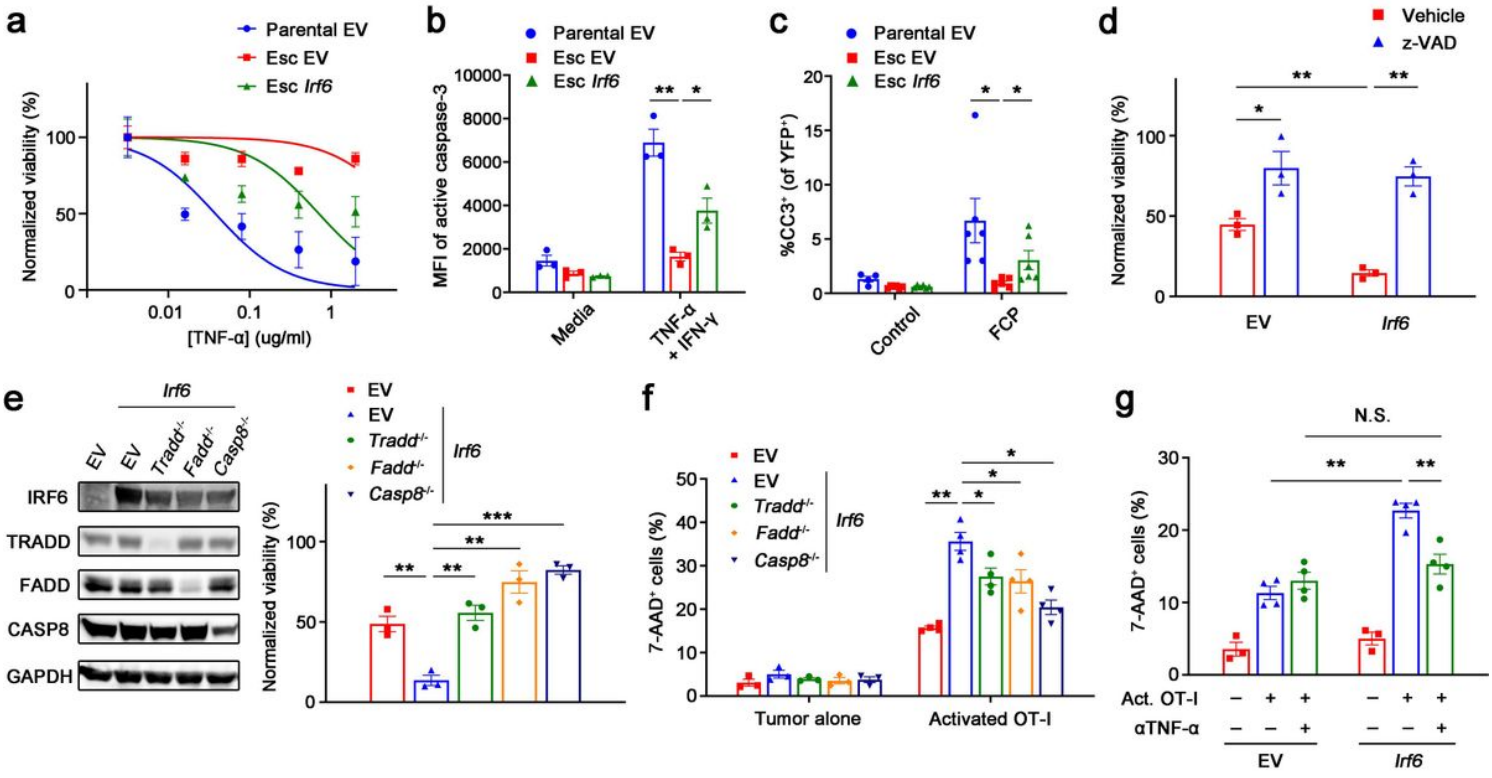

Figure 6

Irf6 promotes susceptibility to T cell killing by enhancing TNF-induced apoptosis. a, Normalized viability of 4662 parental EV, Esc EV, and Esc *Irf6* tumors with varying concentrations of TNF-α in the presence of IFN-γ (0.2 μg/ml) plus cycloheximide (1 μg/ml) for 48 h. IC_{50} values are 0.03472 ug/ml for parental EV, 0.6494 ug/ml for Esc *Irf6*, and not determined for Esc EV tumors. **b**, Mean fluorescence intensities (MFIs) of active caspase-3 in 4662 parental EV, Esc EV, and Esc *Irf6* tumors treated with or without TNF-α (0.5 μg/ml) plus IFN-γ in the presence of cycloheximide for 48 h by flow cytometry. **c**, The percentages of cleaved caspase-3 among s.c. implanted YFP^+ 4662 parental EV, Esc EV, and Esc *Irf6* tumors with or without immunotherapy by IF staining. Tumors were prepared a week after treatment. **d**, Normalized viability of 4662 Esc EV and Esc *Irf6* tumors, treated with vehicle or z-VAD (20 μM), in response to TNF-α plus IFN-γ in the presence of cycloheximide for 48 h. **e**, Left, immunoblots of IRF6 and TNF-related cell

death mediators in 4662 Esc EV and Esc *Irf6* tumors with or without ablation of each gene. Right, normalized viability of 4662 Esc EV and Esc *Irf6* tumors with or without indicated gene ablation in response to TNF-α plus IFN-γ in the presence of cycloheximide for 48 h. **f**, OVA-tdTomato^{+} 4662 Esc EV and Esc *Irf6* tumors with or without indicated gene ablation were used as target cells for OT-I co-culture. **g**, OVA-tdTomato^{+} 4662 Esc EV and Esc *Irf6* tumors were co-cultured with or without activated OT-I and TNF-α neutralizing Ab (5 μg/ml) for 2 d. 7-AAD expression on tumors was measured by flow cytometry. Data represent two independent experiments.

Supplementary Files

This is a list of supplementary files associated with this preprint. Click to download.

- NCOMMS2323245Trs.pdf
- ExtendedDataFiguresNCB.pdf
- SupplementalInformationNCB.pdf